

UNSUPERVISED GEOMETRIC DISENTANGLEMENT FOR SURFACES VIA CFAN-VAE

N. Joseph Tatro

Department of Mathematical Sciences
Rensselaer Polytechnic Institute
Troy, NY 12180
tatron@rpi.edu

Stefan C. Schonsheck

Department of Mathematical Sciences
Rensselaer Polytechnic Institute
Troy, NY 12180
schons@rpi.edu

Rongjie Lai

Department of Mathematical Sciences
Rensselaer Polytechnic Institute
Troy, NY 12180
lair@rpi.edu

May 26, 2020

ABSTRACT

For non-Euclidean data such as meshes of humans, a prominent task for generative models is geometric disentanglement; the separation of latent codes for intrinsic (i.e. identity) and extrinsic (i.e. pose) geometry. This work introduces a novel mesh feature, the conformal factor and normal feature (CFAN), for use in mesh convolutional autoencoders. We further propose CFAN-VAE, a novel architecture that disentangles identity and pose using the CFAN feature and parallel transport convolution. CFAN-VAE achieves this geometric disentanglement in an unsupervised way, as it does not require label information on the identity or pose during training. Our comprehensive experiments, including reconstruction, interpolation, generation, and canonical correlation analysis, validate the effectiveness of the unsupervised geometric disentanglement. We also successfully detect and recover geometric disentanglement in mesh convolutional autoencoders that encode xyz-coordinates directly by registering its latent space to that of CFAN-VAE.

Keywords Geometric deep learning, Deep generative models, Feature disentanglement, Surface analysis, Parallel transport convolution

1 Introduction

Deep learning has shown remarkable success in the fields of computer vision and image analysis. Of recent interest, generative models have proved to be powerful tools for many tasks including synthetic data generation and style transfer. Geometric deep learning is a new field interested in extending the success of deep learning to non-Euclidean structured data [7]. The development of this field is timely given the recent proliferation of point cloud and mesh structured data obtained from sources such as laserscanners [16] and CAD software [9].

Particularly, mesh based convolutional autoencoders (MeshVAEs) are now a popular tool for generating surfaces [11, 26, 29, 34]. These models process a surface via geometric convolutions that respect its intrinsic geometry. With these VAEs achieving state-of-the-art performance on tasks such as reconstruction, more attention is being given towards tasks such as latent space interpretability. Geometric disentanglement, where the latent variables controlling intrinsic (properties independent of surface embedding) and extrinsic (properties dependent on surface embedding) geometry are separated [3], is an important open problem related to such interpretability. Applications of geometric disentanglement include graphics. For instance, it can be desirable to generate synthetic mesh models with either a fixed pose or identity.

Typically, MeshVAEs encode a surface using an input feature that couples intrinsic and extrinsic geometry. In the common case where 3D coordinates are directly encoded, we refer to such networks as xyz-VAEs. Given that it is learned from encoding a feature that entangles intrinsic and extrinsic geometry, it is likely the xyz-VAE latent space is geometrically entangled. Thus we are interested in creating an architecture that explicitly leads to geometric

disentanglement in an unsupervised sense. Namely, we do not require labels for mesh identity and pose. This allows the architecture to be applied more broadly as many mesh datasets do not have meaningful pose labels.

1.1 Related Work

1.1.1 Geometric Convolutional Generative Models

Until fairly recently, the standard technique for generating 3D shapes was through the use of volumetric convolutional neural networks (CNNs) which act on 3D voxels [39, 40]. However, the use of voxels yields coarse representations. Other work has investigated generating surfaces through utilizing point cloud representations. In [2], point clouds of fixed size are generated utilizing the PointNet architecture [10]. A drawback of point clouds is that they lack explicit connectivity between points, thus the structure is not necessarily smooth.

Other work has focused on networks that generate surfaces using non-Euclidean convolutions as part of their architecture. These non-Euclidean convolutions include spectral methods [8, 13, 23], patch based methods [5, 20, 30, 33, 36], and hard-attention methods [6]. In this work, we use the parallel transport convolution (PTC) introduced in [36]. We remark that other convolution operations can be used in the proposed architecture. We do not aim at comparing different geometric convolutions.

There has been extensive research into the construction of generative models using these non-Euclidean convolutions. [26] first proposed to use VAEs to generate 3D meshes. Their proposed network can be used for mesh completion in human bodies, essentially the inpainting problem extended to surfaces. Recently, [34] used a MeshVAE to generate realistic human faces. There has also been recent work in developing generative adversarial networks (MeshGANs): [11] uses a MeshGAN to generate meshes of human faces at high resolution and [29] generates clothes on 3D human bodies.

1.1.2 Geometric Disentanglement

Geometric disentanglement is a popular feature leading to interpretability of the latent space. A typical example is a latent space which separates identity and pose in the case of human body generation [18, 37]. A related but fundamentally different problem is the separation of identity from expression for face generation [1, 19]. This difference arises from the observation that many changes in expression involve relatively large elastic deformations, which conflates intrinsic and extrinsic geometry. Additionally, [18, 19, 37] show that handcrafted feature representations outperform 3D coordinates, advocating for the use of the *as-consistent-as-possible deformation representation* (ACAPDR) introduced in [15]. Recently, [25] proposed a network architecture for supervised geometric disentanglement using non-Euclidean convolution. All these networks involve some kind of supervision to achieve geometric disentanglement; either labels for identity and pose or a mesh in a common reference pose for all identities is required for training.

There has been limited work to achieve unsupervised geometric disentanglement, to eliminate reliance on labeling. To the best of our knowledge, the only previous work on unsupervised geometric disentanglement in 3D data is [3], in which the authors introduce a VAE built on a PointNet architecture [10]. Each point cloud is encoded into a split latent space, representing intrinsic and extrinsic geometric features. The entire latent space is decoded to recover the PointNet features from which the point cloud can be reconstructed. To promote disentanglement, a decoder on the intrinsic geometric latent space is also trained to generate the Laplace-Beltrami eigenvalues. Disentanglement for networks trained on unlabeled data is a topic of interest in general as in [24]. Our method for geometric disentanglement is fundamentally different, being motivated by the Fundamental Theorem of Surfaces [14]. We describe surfaces using conformal factors and surface normal vectors. These features naturally separate intrinsic and extrinsic geometric information and enjoy well established geometric interperability, being easily leveraged by the network architecture we introduce.

1.2 Contributions

To summarize our contributions, in this work, we:

1. introduce a novel mesh feature, the conformal factor and normal feature (CFAN), that decouples intrinsic and extrinsic geometry for use in mesh convolutional autoencoders.
2. propose a novel architecture, CFAN-VAE, for unsupervised geometric disentanglement. For a given mesh, we compute the CFAN feature, and encode its components separately into latent vectors representing intrinsic and extrinsic geometry. We then jointly decode these vectors to the 3D coordinates of the mesh.
3. investigate geometric disentanglement in generic xyz-VAEs by registering this latent space to the disentangled latent space of CFAN-VAE via solving the *Orthogonal Procrustes (OP) problem*. We show that we are able to recover a disentangled latent space for xyz-VAEs without any additional conditions or labels.

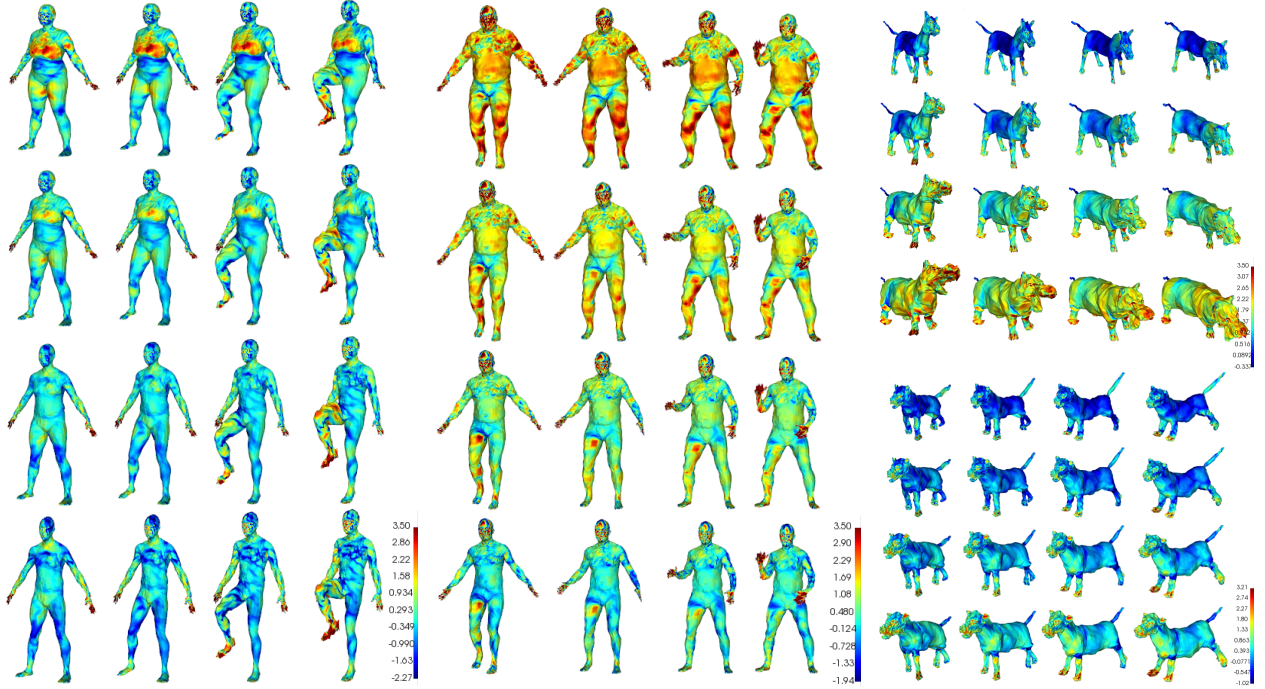


Figure 1: Geometric disentangled interpolations between two meshes from the DFAUST (left and middle) and SMAL (right) datasets. Meshes are generated by CFAN-VAEs with latent dimensions $[16, 16]/[32, 32]$ for DFAUST/SMAL. The horizontal/vertical axis display a linear interpolation in the normal/conformal latent codes, z_n/z_c . The color denotes the pointwise normalized conformal factor computed on each reconstructed mesh. Each row and column corresponds to a specific identity and pose displaying strong geometric disentanglement.

4. perform numerical experiments using two datasets to verify that we achieve geometric disentanglement while maintaining performance on standard metrics.

The rest of this work is organized as follows; we first discuss background on geometric deep learning. Then we introduce our novel mesh signal, the CFAN feature, and architecture, CFAN-VAE. After this, we describe the process of latent space registration for comparing the different latent spaces. Finally, we detail our numerical experiments including reconstruction, interpolation, generation, and latent space analysis.

2 Background on Geometric Deep Learning

Geometric deep learning describes a set of methods used to generalize neural networks to better represent non-Euclidean data (such as manifolds, meshes, and graphs) and incorporate geometric information of this data into the learning process. One common challenge is to define a convolutional operation which is both compatible with the domain and useful in CNNs. This can be challenging because these domains do not have the regularity of Euclidean spaces in which convolution can be computed as a sliding window.

In this work we use Parallel Transport Convolution (PTC), introduced in [36], to construct convolutional layers in our networks. PTC defines a convolution with a compactly supported kernel in \mathbb{R}^2 with a signal supported on a manifold. This is conducted by using parallel transportation, to define a translation-like operation on the tangent space, and the exponential map, to transfer kernels between the tangent space and the manifold. Importantly, all necessary geometric information can be precomputed so that the PTC layer can be implemented as a sparse matrix multiplication with computational costs on the same order as Euclidean convolution (see A.2 for details).

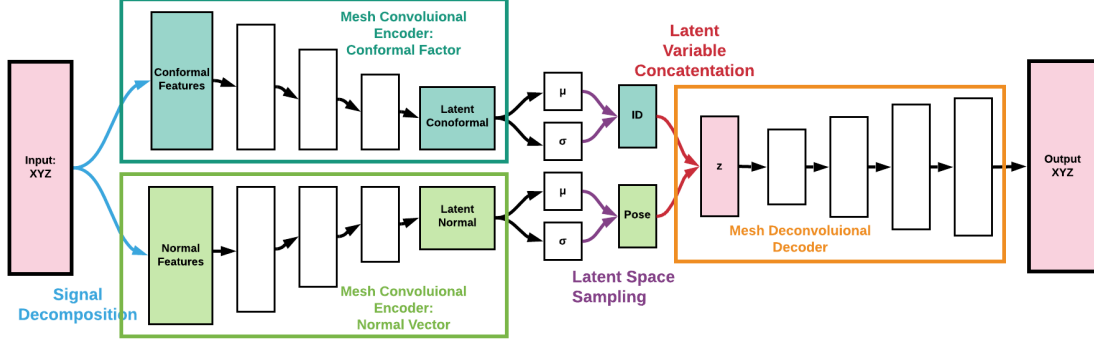


Figure 2: Diagram of the CFAN-VAE network architecture. First, 3D vertex coordinates are transformed into the CFAN feature. This feature is split and encoded to create conformal and normal latent variables, which are jointly decoded to reconstruct the 3D coordinates. The conformal and normal latent variables control identity and pose respectively, leading to geometric disentanglement.

3 CFAN-VAE

Now we introduce our novel architecture for geometric disentanglement, CFAN-VAE. To lead to disentanglement in the latent space, we introduce a feature that decouples intrinsic and extrinsic geometry. We begin by defining the conformal factor and normal (CFAN) feature, which is motivated by this desire as well as the Fundamental Theorem of Surfaces.

3.1 CFAN Feature

The Fundamental Theorem of Surfaces states that a surface can be uniquely reconstructed up to rigid motion given its metric tensor and surface normals, if they satisfy structural conditions known as the Gauss-Codazzi equations [14]. In essence, the metric tensor encapsulates the intrinsic geometry of a surface, while the normals encapsulates the extrinsic. Then we can use metric tensors and normal vector fields to characterize surfaces.

In this work, we restrict ourselves to the study of genus zero surfaces. It is well known that all genus zero surfaces are conformally equivalent [21]. Namely, given two genus-zero surfaces, (\mathcal{M}_1, g_1) and (\mathcal{M}_2, g_2) , there exists a diffeomorphism $\phi : (\mathcal{M}_1, g_1) \rightarrow (\mathcal{M}_2, g_2)$ such that $\phi^*(g_2) = \exp(2\lambda)g_1$. Here the function, λ , is known as the conformal factor and defines a conformal deformation from \mathcal{M}_1 to \mathcal{M}_2 . Then any pair of conformally equivalent surfaces can be deformed into one another (up to isomorphism) by choosing the correct conformal factor. However, in order to properly reconstruct a surface embedded in 3D, we must also fix the isomorphism. This embedding is exactly defined by the surface normal field. These two components define the CFAN feature, with the conformal factor and normal field representing intrinsic and extrinsic geometry respectively.

Given a triangle mesh (X, T) , where $X \in \mathbb{R}^{n \times 3}$ is the set of vertices and $T \in \mathbb{R}^{k \times 3}$ is the corresponding set of faces, we can define the discretized CFAN feature. Each triangle face τ in T has a corresponding face normal \mathbf{n}_τ , where this normal is exterior. We compute the weighted average of these face normals around the first ring structure of each vertex to define a point-wise normal. Since the local area on the surface is given by $\sqrt{\det g}$, it follows that the logarithm of local area is proportional to the conformal factor. Then we define the CFAN feature, (c_i, \mathbf{n}_i) as:

$$c_i := \log \left(\sum_{\tau \in T; i \in \tau} \frac{\text{Area}(\tau)}{3} \right) \quad \mathbf{n}_i := \frac{\sum_{\tau \in T; i \in \tau} \text{Area}(\tau) \mathbf{n}_\tau}{\left\| \sum_{\tau \in T; i \in \tau} \text{Area}(\tau) \mathbf{n}_\tau \right\|} \quad (1)$$

Compared to other popular features, such as the previously mentioned ACAPDR or SHOT descriptors [38], the CFAN feature is easier to compute and more compact. In practice, we perform a pointwise normalization of these features before using them as input into the network.

3.2 Network Architecture

With the CFAN feature defined, we propose a simple and easy-to-implement architecture, CFAN-VAE, as shown in Figure 2 to achieve unsupervised geometric disentanglement. The intuition behind the architecture is to encode the conformal factor and the normal features separately. The 3D vertex coordinates of an input mesh under some fixed

triangulation are first converted to the CFAN feature. Then, the feature components are separately encoded to create two different latent variables, the conformal latent variable z_c and the normal latent variable z_n in the disentangled latent space $\mathbf{Z}_{c,n} = \mathbf{Z}_c \times \mathbf{Z}_n$. As a result, z_c corresponds to intrinsic geometric information, controlling surface identity, and z_n corresponds to extrinsic geometric information, controlling surface pose. After that, the CFAN latent variable $z_{c,n} = [z_c, z_n] \in \mathbf{Z}_{c,n}$ is decoded to obtain the reconstructed 3D coordinates.

Our model is built on geometric convolution given by PTC layers. To follow convention for convolutional VAEs, the mesh signal is decimated during encoding and refined during decoding. To be clear, for each convolution layer we define subsets, source vertices and target vertices. The convolution is performed at each target vertex, where its neighborhood support is restricted to the source vertices. During encoding/decoding, the target vertices are determined by down/up-sampling the source vertices by a factor of four. This sampling is precomputed by the Farthest Point Sampling (FPS) method in Euclidean space [32], which serves as a fast approximation to a geodesic FPS, though the quality of the sampling deteriorates with the level of decimation. After the final mesh convolution in the encoder, dense layers map the signal to the variational statistics, with $\mu_{c,n} := [\mu_c, \mu_n]$ and $\sigma_{c,n} := [\sigma_c, \sigma_n]$ denoting the mean and variance. A dense layer also maps $z_{c,n}$ to the first mesh signal in the decoder.

3.3 Loss Function

The training loss for our model is given by:

$$L(X, X') := \|X - X'\|_1 + \lambda_{KL} \|\sigma_{c,n}^2 + \mu_{c,n}^2 - 1 - \log(\sigma_{c,n}^2)\|_1 \quad (2)$$

where X is the input, X' is the network output, and $\mu_{c,n}$ and $\sigma_{c,n}^2$ are the mean and covariance of the latent posterior. The first term is simply the L_1 error of the 3D coordinates. This promotes an objective function that is robust to vertex outliers which is generally more visually pleasing than using L_2 error. The second term of the loss function is the KL-divergence of the latent representation from the unit normal distribution, given by the Bayesian prior assumption [22].

3.3.1 Linearized Jacobian Norm Penalty

In CFAN-VAE, geometric disentanglement is a result of separately encoding intrinsic geometric information and extrinsic geometric information that together determine a surface. We stress that structural conditions given by the Gauss-Codazzi equations prevent guaranteeing complete independence of the separate latent vectors. In many ways this is intuitive, considering motion can be restricted by intrinsic properties such as body mass distribution. In light of this, we use a linearization of the Jacobian norm penalty [3] to promote independence. Letting q_c and q_n denote the conformal and normal encoders and p denote the decoder, the Linearized Jacobian Norm penalty is:

$$L_{LJN} = \frac{\|\mu_c - q_c(p([\mu_c, \mu_n + \sigma_n \epsilon]))\|^2}{\|\sigma_n \epsilon\|^2} + \frac{\|\mu_n - q_n(p([\mu_c + \sigma_c \epsilon, \mu_n]))\|^2}{\|\sigma_c \epsilon\|^2}, \quad (3)$$

where $\epsilon \sim \mathcal{N}(0, 2)$. The noise is chosen so that it is more diffuse, and thus distinguishable, from the noise associated with the KL-divergence loss of the VAE. Assuming perfect reconstruction by the VAE, this regularization term penalizes the change in the conformal/normal latent variable upon re-encoding with respect to a change in the other latent variable. This promotes the geometric disentanglement we are interested in.

4 Latent Space Registration

A natural question is to what extent CFAN-VAE can provide insight on the entanglement in xyz-VAEs and disentangle them. We explore this through Orthogonal Procrustes (OP) analysis [35] and conclude that disentanglement is indeed possible without using label information.

Normally, the goal of OP analysis is to register two datasets through an orthonormal transformation. Here, we register two separate latent representations of the same dataset, one encoded by a xyz-VAE and one by a CFAN-VAE. Let \mathbf{Z}_x and $\mathbf{Z}_{c,n}$, both in $\mathbb{R}^{n \times k}$, be the latent embeddings from the xyz-VAE and the CFAN-VAE models where n and k denote the number of data samples and the latent dimension respectively. Then the OP problem is:

$$\mathbf{R}^* = \arg \min_{\mathbf{R} \in SO(k)} \|\mathbf{Z}_x \mathbf{R} - \mathbf{Z}_{c,n}\|_F^2 = \mathbf{U} \mathbf{V}^T \quad (4)$$

where \mathbf{U}, \mathbf{V} are provided from a singular value decomposition $\mathbf{Z}_x^T \mathbf{Z}_{c,n} = \mathbf{U} \mathbf{\Sigma} \mathbf{V}^T$. Essentially, we are searching for the optimal rotation that aligns the xyz-VAE latent embedding of the dataset to the CFAN-VAE latent embedding.

Since $\mathbf{Z}_{c,n}$ is the concatenation of the conformal and normal latent codes, we write $\mathbf{R}^* = [\mathbf{R}_c^* | \mathbf{R}_n^*]$ as two matrices concatenated along the column dimension. This allows us to define latent subspaces:

$$\mathbf{Z}_{x,c} = \mathbf{Z}_x \mathbf{R}_c^*, \quad \mathbf{Z}_{x,n} = \mathbf{Z}_x \mathbf{R}_n^*, \quad \text{where} \quad \mathbf{R}^* = [\mathbf{R}_c^* | \mathbf{R}_n^*]. \quad (5)$$

Thus, we identify corresponding conformal and normal latent codes in the xyz-VAE latent space: $z_{x,c}$ and $z_{x,n}$. In section 5.2.4, we will demonstrate these latent subspaces identified through registration exhibit significant geometric disentanglement.

5 Numerical Experiments

We demonstrate the efficacy of the CFAN-VAE through a set of numerical experiments including reconstruction, interpolation, generation, and latent space analysis. For comparison, we also train an xyz-VAE, which directly encodes 3D coordinates, with a similar architecture and number of parameters. Finally, we show how a CFAN-VAE can be used to disentangle the latent space of a xyz-VAE. All numerical experiments are conducted on a desktop with three NVIDIA 2080 Ti GPUs.

5.1 Experimental Setup

5.1.1 Datasets

We consider two datasets in our experiments. The first is the DFAUST, a real world dataset containing a set of 10 people captured in motion performing several poses [4]. We randomly split the dataset into a training/validation/test set of 35,720/500/5,000 meshes respectively.

For additional data, we generated a synthetic dataset of animals referred to as SMAL following [41], which uses the SMPL model introduced in [27]. This set contains five classes of animals of 20 shape and 200 pose variations each. We randomly split the set into a training/validation/test set of 17,000/500/2,500 meshes. Additional details on the generation can be found in section C.

5.1.2 Architecture Hyperparameters

Each VAE contains a 4 layer encoder and a 4 layer decoder. For CFAN-VAE trained on DFAUST, the conformal factor encoder and the normal encoder have the same number of kernels at each layer, [12, 24, 24, 48]. For xyz-VAE trained on DFAUST, the encoder has the number of kernels, [16, 32, 32, 64]. Both networks have a decoder with the number of kernels, [64, 32, 32, 16]. For SMAL, these hyperparameters are [24, 48, 48, 48], [32, 64, 64, 64], and [64, 64, 64, 32] respectively. For the PTC kernels, we use a 13 point stencil with a initial kernel radius of 50mm. During encoding/decoding, this radius is respectively increased/reduced by a factor of 2 at each consecutive layer. For latent dimensions in CFAN-VAE, we consider three cases; [8, 8], [16, 16], and [32, 32] sizes for the conformal/normal latent vectors. For xyz-VAE, we consider comparable latent dimension cases; 16, 32, and 64.

We use batch normalization (BN) layers in the encoder to prevent the loss from diverging during training. The decoder does not contain BN layers as this would exacerbate the stochastic nature of the optimization. When training with the linearized jacobian norm penalty, we freeze the BN layers during reencoding. The activation function for the encoder is ReLU and is ELU for the decoder. We use the AdamW optimizer [28] with a learning rate of 1E-3 and a weight decay of 5E-5. The value of λ_{KL} is chosen to be 1E-3. For DFAUST and SMAL, λ_{LJN} is set to 1E-5 and 1E-4 respectively. Each model is trained for 300 epochs with a batch size of 32. We train three instances of each network using different three fixed random seeds.

5.2 Results

5.2.1 Surface Reconstruction

First we verify that CFAN-VAE is able to accurately reconstruct surfaces. Figure 3 displays high quality reconstructions for each dataset using CFAN-VAEs with conformal/normal latent dimensions of [16, 16] and [32, 32] for DFAUST and SMAL respectively. Table 1 contains quantitative measurements related to the performance for each CFAN-VAE and xyz-VAE. This includes L_1 reconstruction error and KL divergence, as well as the generalization error (mm) on the test sets. The generalization error is the average L_2 vertex error on the reconstruction. Clearly CFAN-VAE can reconstruct high quality meshes, though it is slightly outperformed by the corresponding xyz-VAE. This can be seen as the cost of unsupervised geometric disentanglement. We note that this cost decreases with respect to latent dimension. In terms of

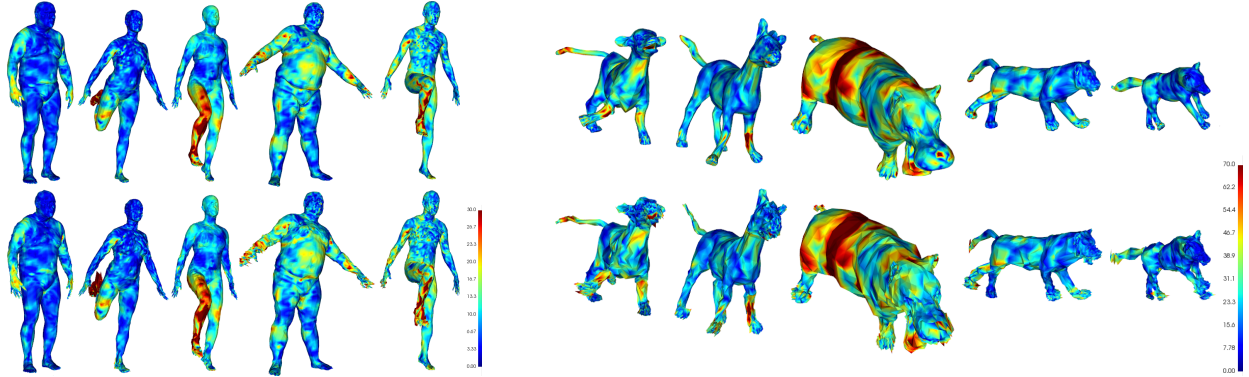


Figure 3: Reconstructions from the CFAN-VAE models in Figure 1. The mesh color represents the pointwise Euclidean error in the reconstructed coordinate. The top row are the ground truth meshes, and the bottom row are the reconstructions. Then, CFAN-VAE can reliably reconstruct the mesh. Qualitatively, these reconstructions are comparable to xyz-VAE reconstructions as seen in Figure 5.

Table 1: The L1 reconstruction loss, KL divergence loss, and the generalization error (mm) on the test set for each trained model.

Dataset	#z	xyz-VAE			CFAN-VAE		
		L1 (E-1)	KLD (E1)	Error (mm)	L1 (E-1)	KLD (E1)	Error (mm)
DFAUST	16	2.35 ± 0.02	5.64 ± 0.25	13.53 ± 0.11	2.78 ± 0.02	5.18 ± 0.04	16.01 ± 0.10
	32	1.85 ± 0.01	8.03 ± 0.01	10.67 ± 0.07	2.31 ± 0.02	7.60 ± 0.08	13.26 ± 0.11
	64	1.89 ± 0.01	7.93 ± 0.02	10.89 ± 0.06	2.24 ± 0.03	8.25 ± 0.03	12.88 ± 0.18
SMAL	16	1.32 ± 0.01	5.50 ± 0.06	27.77 ± 0.14	1.39 ± 0.02	4.75 ± 0.01	29.17 ± 0.36
	32	1.16 ± 0.00	6.77 ± 0.01	24.50 ± 0.10	1.22 ± 0.01	6.34 ± 0.02	25.57 ± 0.21
	64	1.16 ± 0.00	6.84 ± 0.02	24.41 ± 0.02	1.17 ± 0.01	6.72 ± 0.05	24.57 ± 0.14

latent dimension, we find that there is only a marginal reduction in generalization error from the 32 dimensional latent space models to the 64 dimensional latent space models, as KL divergence loss begins to dominate.

We remark that reconstructions of surfaces of extreme identity or pose are prone to some error. For instance, the waist of the hippos in SMAL or the right foot when raised behind in DFAUST are outliers. We stress that these errors are not unique to CFAN-VAE, as these errors are also present in xyz-VAE reconstructions. Such error can be addressed by wider networks (i.e. more filters), though this is computationally intensive.

5.2.2 Surface Interpolation

Interpolating between data is a popular task for VAEs. To achieve this, we simply encode two data, linearly interpolate between their latent code, and decode this interpolation. A similar problem is that of style transfer. To this end, we wish to smoothly transfer the pose or identity of one mesh onto another while keeping the other property fixed. Geometric disentanglement from CFAN-VAE provides a successful way to do this. For instance, transferring identity can be achieved via interpolating the conformal latent codes, z_c , while keeping the normal latent codes, z_n , fixed. Transferring pose is analogous.

Figure 1 displays examples of such interpolations for each dataset using CFAN-VAE. In this figure, the vertical and horizontal axis represents conformal and normal interpolations respectively. The colormap denotes the pointwise normalized conformal factor of the reconstructions. These numerical results verify that the proposed CFAN-VAE produces meaningful geometric disentanglement between intrinsic and extrinsic information. Thus, it enjoys flexibility to generate high quality meshes preserving either identity or pose. We stress that visually this disentanglement is quite compelling. Notice, the colormaps and position are almost identical for fixed identity and pose respectively. We include additional examples of disentangled interpolation in Appendix D.

We further compute metrics for quantitatively confirming the ability of CFAN-VAE to perform transfer tasks. For judging pose transfer, we confirm that identity is preserved by measuring the squared relative distance between the Laplace-Beltrami eigenvalues of the two meshes using the weighted norm in [12]. For judging identity transfer, we compute the median cosine distance between the surface normals of the two meshes to confirm that the pose is similar.

Table 2: Distance metrics describing the pose and identity transfer tasks completed by CFAN-VAE. The source and target meshes are constructed from the latent variables, $[z_c^{(1)}, z_n^{(1)}]$ and $[z_c^{(2)}, z_n^{(2)}]$, respectively. We exchange these latent codes to complete either pose or identity transfer with respect to the first surface. The pose transfer is measured with respect to a distance on the Laplace-Beltrami eigenvalues and the identity transfer is measured using a cosine distance on the surface normals. These distances are the mean over 100 mesh pairs.

Identity	Pose	DFAUST		SMAL	
		Eigen Dist.	Cos Dist.	Eigen Dist.	Cos Dist.
$z_c^{(1)}$	$z_n^{(1)}$	0.000	0.000	0.000	0.000
$z_c^{(1)}$	$z_n^{(2)}$	0.051 ± 0.000	-	0.074 ± 0.000	-
$z_c^{(2)}$	$z_n^{(1)}$	-	0.270 ± 0.001	-	0.440 ± 0.003
$z_c^{(2)}$	$z_n^{(2)}$	0.184 ± 0.003	0.357 ± 0.004	0.603 ± 0.000	0.727 ± 0.005

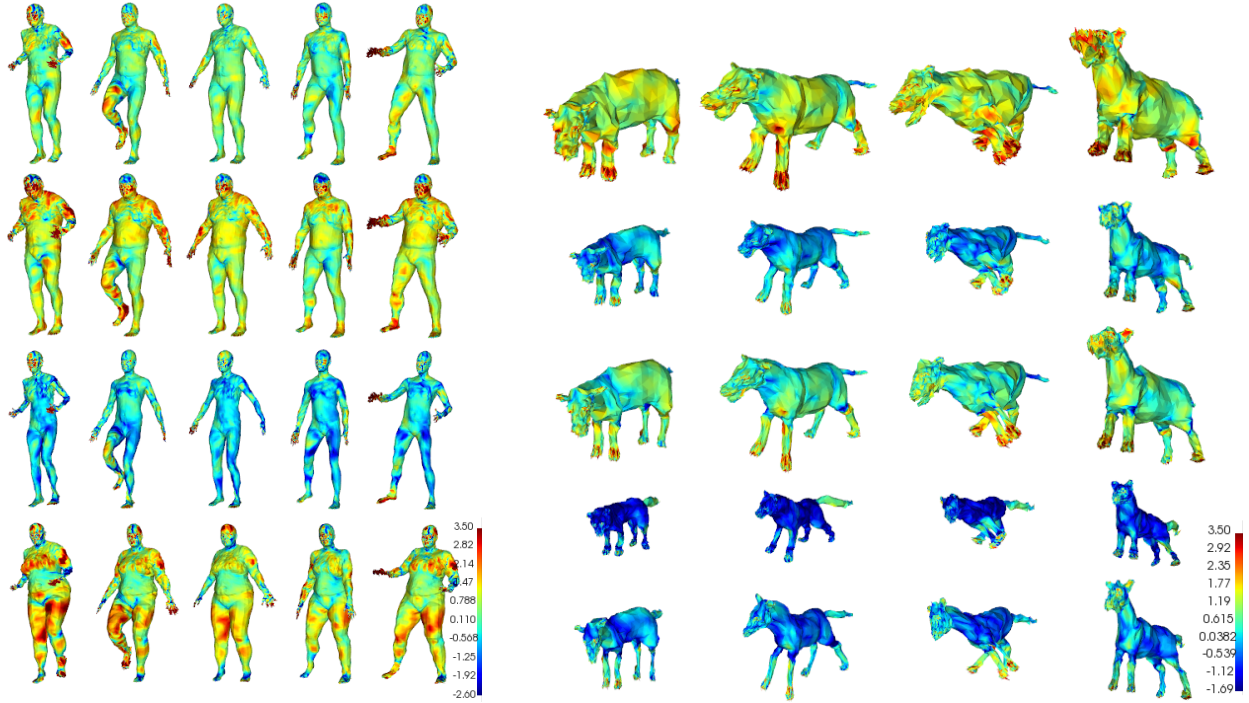


Figure 4: **Left/Right:** DFAUST/SMAL surfaces generated by sampling the CFAN-VAE latent space, using $N(0, 0.8)$ for each variable. The horizontal and vertical axes correspond to z_n and z_c respectively. Mesh color corresponds to the pointwise normalized conformal factor of the generation. Clearly, CFAN-VAE reliably generates meshes in a specific pose or with nearly the same identity, showing geometric disentanglement.

Table 2 clearly shows that CFAN-VAE successfully and smoothly transfers identity and pose. This nice property of the CFAN-VAE latent space enables flexible control of intrinsic and extrinsic information of generated surfaces.

5.2.3 Surface Generation

Another typical task for VAEs is the generation of new surfaces via decoding samples the latent space following the variational prior. Since the goal of CFAN-VAE is to achieve geometric disentanglement, we expect that we should be able to randomly generate surfaces of different identity with the same pose or surfaces in the different poses with the same identity. This is accomplished through separate samplings of conformal latent code z_c and normal latent code z_n .

Figure 4 plots examples of such random generations where latent codes are sampled from $N(0, 0.8)$. Here the normal latent code and conformal code is fixed along the vertical axis and horizontal axis, respectively. Clearly, pose and identity are successfully fixed respectively. We note that the generated meshes are of comparable visual quality to the reconstructions from the test set. Then the latent space of CFAN-VAE allows for successful high-quality surface generation while providing interpretability of geometric features.

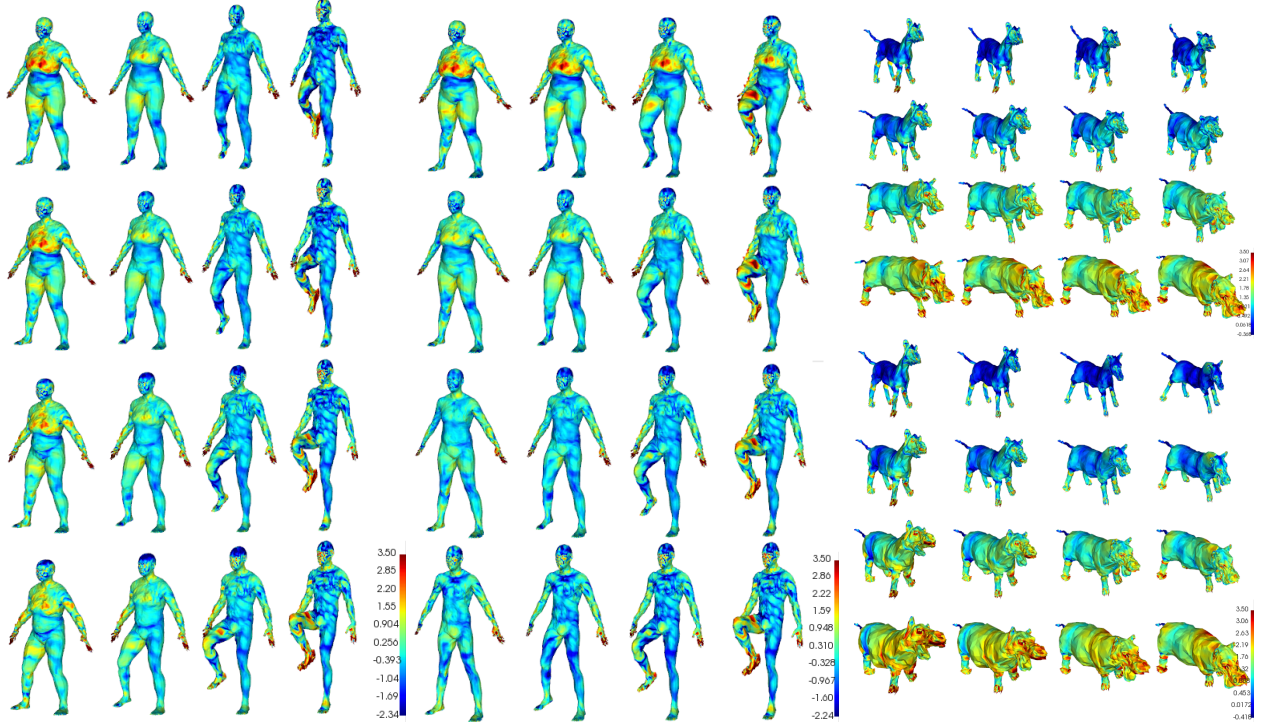


Figure 5: **Left/Top Right:** Analogous interpolations for a xyz-VAE compared to those in Figure 1 with latent dimension 32/64 for the DFAUST/SMAL datasets. Here the horizontal/vertical axis corresponds to the first/last half of latent variables. This emphasizes that a naive split of the latent space of an xyz-VAE entangles intrinsic and extrinsic geometry. **Middle/Bottom Right:** Interpolations for the same xyz-VAE, using latent variables, $z_{x,n}$ and $z_{x,c}$ determined by OP registration of the latent space, Z_x , to that of the CFAN-VAE. Then we see a strong presence of geometric disentanglement in xyz-VAEs.

5.2.4 Latent Registration

A natural question to ask is how the CFAN-VAE and xyz-VAE latent spaces are related. As previously discussed, from Table 1 there is a trade-off between generalization error and unsupervised geometric disentanglement provided by training the CFAN-VAE. Through an OP registration between the latent spaces of xyz-VAE and CFAN-VAE, we detect some disentanglement in xyz-VAE without needing supervision. This provides interpretability of the xyz-VAE latent space while allowing us to better balance this trade-off.

We verify the ability to disentangle xyz-VAE latent space using CFAN-VAE in Figure 5. In the middle and bottom right panels, we display the interpolations using the registered xyz-VAE latent space based on equation 5. There is clear geometric disentanglement, although still some unavoidable entanglement. For example, in the rightmost column for the DFAUST interpolation, the foot is not always in the exact same position for the xyz-VAE. Notably, this is not a problem for the same interpolation using the CFAN-VAE in Figure 1. It is significant that CFAN-VAE can identify geometric disentanglement in a network that is trained without disentanglement as a goal. For comparison, we include naive interpolations using unregistered latent variables in xyz-VAE latent space in the left and top right panels of Figure 5. The natural latent variables (i.e. standard basis) learned from a xyz-VAE entangle intrinsic and extrinsic geometry, but we are able to use the CFAN-VAE to identify disentangled variables.

5.3 Latent Space Analysis

To better assess the presence of geometric disentanglement in xyz-VAEs, we analyze the latent spaces of the CFAN-VAEs and xyz-VAEs after OP registration. Given perfect disentanglement, we expect identity clusters to be detectable in the conformal latent embeddings but not the normal latent embeddings. Similarly, we expect that pose clusters are detectable in normal latent embeddings but not in conformal latent embeddings. In Figure 6, we visualize both the clustering in these networks and the registration of the xyz-VAE to a CFAN-VAE using canonical correlation analysis (CCA). For either the conformal or normal subspaces in CFAN-VAE and xyz-VAE, this method finds the two linear

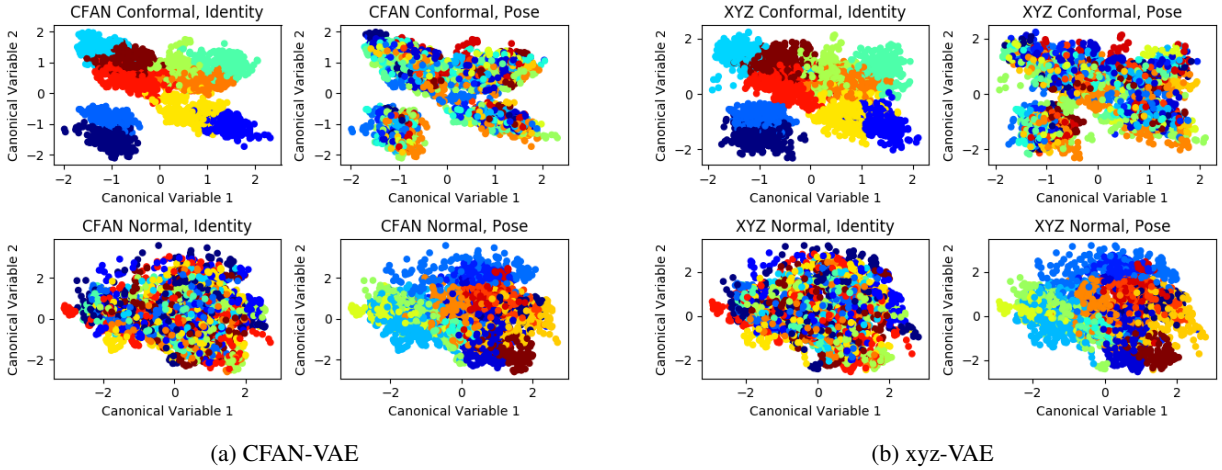


Figure 6: A canonical correlation analysis (CCA) of registered latent spaces. The network is the aforementioned CFAN-VAE/xyz-VAE trained on DFAUST. CCA is performed for the pairs, $z_c/z_{x,c}$ (top rows) and $z_n/z_{x,n}$ (bottom rows). These plots are a 2D CCA embedding of the latent spaces. The color in the left/right columns denotes the identity/pose associated with the embedded mesh. Clearly, the conformal latent vectors encode identity but do not encode pose, and the normal latent vectors encode pose but do not encode identity.

Table 3: The Davies-Bouldin index (DBI) for identity and pose clusters associated with the specified latent embedding for the DFAUST networks. The latents, $z_{x,c}$ and $z_{x,n}$, are computed through the OP registration of z_x to $z_{c,n}$.

Latent Variable	Total Latent Dimension					
	16		32		64	
	Identity	Pose	Identity	Pose	Identity	Pose
z_x	2.79 ± 0.01	5.03 ± 0.10	3.13 ± 0.01	4.54 ± 0.01	3.09 ± 0.01	4.64 ± 0.01
$z_{x,c}$	2.03 ± 0.06	7.78 ± 0.06	2.48 ± 0.01	7.56 ± 0.07	3.96 ± 0.14	8.50 ± 0.18
$z_{x,n}$	7.09 ± 0.10	3.97 ± 0.15	6.13 ± 0.03	4.25 ± 0.04	5.69 ± 0.17	4.93 ± 0.11
$z_{c,n}$	2.57 ± 0.01	4.54 ± 0.02	2.70 ± 0.03	4.52 ± 0.05	2.97 ± 0.03	4.71 ± 0.03
z_c	1.72 ± 0.04	7.52 ± 0.03	1.98 ± 0.03	7.85 ± 0.28	3.68 ± 0.05	9.94 ± 0.28
z_n	6.38 ± 0.03	3.85 ± 0.02	5.86 ± 0.12	4.26 ± 0.03	4.98 ± 0.05	4.65 ± 0.08

transformations that whiten the individual data embeddings, while maximizing their cross-correlation. We refer to [17] for details on CCA. Then these provide embeddings in the CFAN-VAE and xyz-VAE latent spaces which are maximally correlated. We see that our expectations of clustering are met in this visualization; identity clusters only exist in the conformal embeddings and pose clusters only exist in the normal embeddings. Additionally, it is visually clear that the CFAN-VAE and xyz-VAE embeddings are incredibly similar. This implies that the latent spaces of these different architectures are highly correlated and are in meaningful linear correspondence.

To measure the quality of clustering, we use the Davies-Bouldin Index (DBI) as described in [31]. This metric essentially measures the average worst scenario in terms of linear separation between two clusters, with a lower index denoting better clustering. We find linear clustering metrics to be appropriate as operations in the latent space are linear in many applications. Table 3 contains the DBI for all trained networks on the DFAUST dataset. It is clear that the DBI is usually lowest for identity clusters in conformal latent spaces and pose clusters in normal latent spaces. Additionally, the DBI is highest for identity clusters in normal latent space and pose clusters in conformal latent space. These results strongly support the existence of geometric disentanglement in CFAN-VAEs. Moreover, it is evident that some level of geometric disentanglement is detectable and achievable in xyz-VAEs through registration to a similar CFAN-VAE.

6 Conclusion

In this work, we propose a novel architecture for unsupervised geometric disentanglement in mesh convolutional autoencoders. This is accomplished by first transforming 3D coordinates of the mesh vertices to a conformal factor and normal (CFAN) feature. This feature is then separately encoded to produce conformal and normal latent vectors, thus separating intrinsic and extrinsic geometry, that is jointly decoded to recover 3D coordinates. There is clearly

strong geometric disentanglement in CFAN-VAEs. Additionally, we successfully detect geometric disentanglement in xyz-VAEs by registering their latent spaces to those of CFAN-VAEs. The continued integration of geometric theory into neural network architectures can only lead to more interesting results in the future.

Acknowledgements

J. Tatro and R. Lai’s work is supported in part by NSF CAREER Award (DMS—1752934). J. Tatro’s work is also supported in part by IBM-RPI AIRC program. Part of this research was performed while the authors were visiting the Institute for Pure and Applied Mathematics (IPAM), which is supported by the NSF DMS-1440415, during the *Geometry and Learning from Data in 3D and Beyond* long program.

References

- [1] Abrevaya, V.F., Boukhayma, A., Wuhler, S., Boyer, E.: A decoupled 3d facial shape model by adversarial training (2019)
- [2] Achlioptas, P., Diamanti, O., Mitliagkas, I., Guibas, L.: Learning representations and generative models for 3d point clouds (2017)
- [3] Aumentado-Armstrong, T., Tsogkas, S., Jepson, A., Dickinson, S.: Geometric disentanglement for generative latent shape models (2019)
- [4] Bogo, F., Romero, J., Pons-Moll, G., Black, M.J.: Dynamic FAUST: Registering human bodies in motion. In: IEEE Conf. on Computer Vision and Pattern Recognition (CVPR) (Jul 2017)
- [5] Boscaini, D., Masci, J., Rodolà, E., Bronstein, M.: Learning shape correspondence with anisotropic convolutional neural networks. In: Advances in Neural Information Processing Systems. pp. 3189–3197 (2016)
- [6] Bouritsas, G., Bokhnyak, S., Ploumpis, S., Bronstein, M., Zafeiriou, S.: Neural 3d morphable models: Spiral convolutional networks for 3d shape representation learning and generation (2019)
- [7] Bronstein, M.M., Bruna, J., LeCun, Y., Szlam, A., Vandergheynst, P.: Geometric deep learning: Going beyond euclidean data. IEEE Signal Processing Magazine **34**(4), 18–42 (Jul 2017). <https://doi.org/10.1109/msp.2017.2693418>, <http://dx.doi.org/10.1109/MSP.2017.2693418>
- [8] Bruna, J., Zaremba, W., Szlam, A., LeCun, Y.: Spectral networks and locally connected networks on graphs (2013)
- [9] Chang, A.X., Funkhouser, T., Guibas, L., Hanrahan, P., Huang, Q., Li, Z., Savarese, S., Savva, M., Song, S., Su, H., et al.: Shapenet: An information-rich 3d model repository. arXiv preprint arXiv:1512.03012 (2015)
- [10] Charles, R.Q., Su, H., Kaichun, M., Guibas, L.J.: Pointnet: Deep learning on point sets for 3d classification and segmentation. 2017 IEEE Conference on Computer Vision and Pattern Recognition (CVPR) (Jul 2017). <https://doi.org/10.1109/cvpr.2017.16>, <http://dx.doi.org/10.1109/cvpr.2017.16>
- [11] Cheng, S., Bronstein, M., Zhou, Y., Kotsia, I., Pantic, M., Zafeiriou, S.: Meshgan: Non-linear 3d morphable models of faces (2019)
- [12] Cosmo, L., Panine, M., Rampini, A., Ovsjanikov, M., Bronstein, M.M., Rodolà, E.: Isospectralization, or how to hear shape, style, and correspondence. In: Proceedings of the IEEE Conference on Computer Vision and Pattern Recognition. pp. 7529–7538 (2019)
- [13] Defferrard, M., Bresson, X., Vandergheynst, P.: Convolutional neural networks on graphs with fast localized spectral filtering. In: Advances in neural information processing systems. pp. 3844–3852 (2016)
- [14] Do Carmo, M.P.: Differential Geometry of Curves and Surfaces: Revised and Updated Second Edition. Courier Dover Publications (2016)
- [15] Gao, L., Lai, Y.K., Yang, J., Ling-Xiao, Z., Xia, S., Kobbelt, L.: Sparse data driven mesh deformation. IEEE Transactions on Visualization and Computer Graphics p. 1–1 (2019). <https://doi.org/10.1109/tvcg.2019.2941200>, <http://dx.doi.org/10.1109/tvcg.2019.2941200>
- [16] Geiger, A., Lenz, P., Stiller, C., Urtasun, R.: Vision meets robotics: The kitti dataset. International Journal of Robotics Research (IJRR) (2013)
- [17] Hardoon, D.R., Szedmak, S., Shawe-Taylor, J.: Canonical correlation analysis: An overview with application to learning methods. Neural computation **16**(12), 2639–2664 (2004)
- [18] Jiang, B., Zhang, J., Cai, J., Zheng, J.: Learning 3d human body embedding (2019)

- [19] Jiang, Z.H., Wu, Q., Chen, K., Zhang, J.: Disentangled representation learning for 3d face shape (2019)
- [20] Jin, P., Lai, T., Lai, R., Dong, B.: Nptc-net: Narrow-band parallel transport convolutional neural network on point clouds. arXiv preprint arXiv:1905.12218 (2019)
- [21] Jost, J., Jost, J.: Riemannian geometry and geometric analysis, vol. 42005. Springer (2008)
- [22] Kingma, D.P., Welling, M.: Auto-encoding variational bayes. arXiv preprint arXiv:1312.6114 (2013)
- [23] Kipf, T.N., Welling, M.: Semi-supervised classification with graph convolutional networks (2016)
- [24] Kumar, A., Sattigeri, P., Balakrishnan, A.: Variational inference of disentangled latent concepts from unlabeled observations (2017)
- [25] Levinson, J., Sud, A., Makadia, A.: Latent feature disentanglement for 3d meshes (2019)
- [26] Litany, O., Bronstein, A., Bronstein, M., Makadia, A.: Deformable shape completion with graph convolutional autoencoders. 2018 IEEE/CVF Conference on Computer Vision and Pattern Recognition (Jun 2018). <https://doi.org/10.1109/cvpr.2018.00202>, <http://dx.doi.org/10.1109/CVPR.2018.00202>
- [27] Loper, M., Mahmood, N., Romero, J., Pons-Moll, G., Black, M.J.: Smpl: a skinned multi-person linear model. ACM Trans. Graph. **34**, 248:1–248:16 (2015)
- [28] Loshchilov, I., Hutter, F.: Decoupled weight decay regularization. arXiv preprint arXiv:1711.05101 (2017)
- [29] Ma, Q., Tang, S., Pujades, S., Pons-Moll, G., Ranjan, A., Black, M.J.: Dressing 3d humans using a conditional mesh-vae-gan. ArXiv **abs/1907.13615** (2019)
- [30] Masci, J., Boscaini, D., Bronstein, M.M., Vandergheynst, P.: Geodesic convolutional neural networks on riemannian manifolds. 2015 IEEE International Conference on Computer Vision Workshop (ICCVW) (Dec 2015). <https://doi.org/10.1109/iccvw.2015.112>, <http://dx.doi.org/10.1109/ICCVW.2015.112>
- [31] Maulik, U., Bandyopadhyay, S.: Performance evaluation of some clustering algorithms and validity indices. IEEE Transactions on pattern analysis and machine intelligence **24**(12), 1650–1654 (2002)
- [32] Moenning, C., Dodgson, N.A.: Fast marching farthest point sampling. Tech. rep., University of Cambridge, Computer Laboratory (2003)
- [33] Monti, F., Boscaini, D., Masci, J., Rodola, E., Svoboda, J., Bronstein, M.M.: Geometric deep learning on graphs and manifolds using mixture model cnns. 2017 IEEE Conference on Computer Vision and Pattern Recognition (CVPR) (Jul 2017). <https://doi.org/10.1109/cvpr.2017.576>, <http://dx.doi.org/10.1109/cvpr.2017.576>
- [34] Ranjan, A., Bolkart, T., Sanyal, S., Black, M.J.: Generating 3d faces using convolutional mesh autoencoders. Lecture Notes in Computer Science p. 725–741 (2018)
- [35] Schönemann, P.H.: A generalized solution of the orthogonal procrustes problem. Psychometrika **31**(1), 1–10 (1966)
- [36] Schonsheck, S.C., Dong, B., Lai, R.: Parallel transport convolution: A new tool for convolutional neural networks on manifolds (2018)
- [37] Tan, Q., Gao, L., Lai, Y.K., Xia, S.: Variational autoencoders for deforming 3d mesh models. 2018 IEEE/CVF Conference on Computer Vision and Pattern Recognition (Jun 2018). <https://doi.org/10.1109/cvpr.2018.00612>, <http://dx.doi.org/10.1109/cvpr.2018.00612>
- [38] Tombari, F., Salti, S., Di Stefano, L.: Unique signatures of histograms for local surface description. In: European conference on computer vision. pp. 356–369. Springer (2010)
- [39] Wu, J., Zhang, C., Xue, T., Freeman, W.T., Tenenbaum, J.B.: Learning a probabilistic latent space of object shapes via 3d generative-adversarial modeling (2016)
- [40] Wu, Z., Song, S., Khosla, A., Yu, F., Zhang, L., Tang, X., Xiao, J.: 3d shapenets: A deep representation for volumetric shapes. 2015 IEEE Conference on Computer Vision and Pattern Recognition (CVPR) (Jun 2015). <https://doi.org/10.1109/cvpr.2015.7298801>, <http://dx.doi.org/10.1109/CVPR.2015.7298801>
- [41] Zuffi, S., Kanazawa, A., Jacobs, D., Black, M.J.: 3D menagerie: Modeling the 3D shape and pose of animals. In: IEEE Conf. on Computer Vision and Pattern Recognition (CVPR) (Jul 2017)

Appendix

A Background

In this section we review background on variational autoencoders and geometric deep learning.

A.1 Variational Autoencoders

The variational autoencoder (VAE) is a deep generative model introduced in [22]. Assume the input into the generative model is $x \in \mathbb{R}^n$. Then the VAE consists of a probabilistic encoder, $q_\theta(z|x_i)$, and a probabilistic decoder, $p_\phi(x_i|z)$. Here, we have the latent variable, $z \sim q_\theta(z|x_i)$, as well as the reconstruction \hat{x} , where $\hat{x}_i \sim p_\phi(x_i|z)$. We also assume a prior distribution, $p(z)$, on the latent variable.

The VAE loss is described in equation 6 below. This loss is composed of the negative log likelihood of the reconstruction and the KL divergence of the variational posterior from the prior on the latent variable.

$$\mathcal{L}(\theta, \phi) = \sum_{i=1}^n -\mathbb{E}_{z \sim q_\theta(z|x_i)} [\log p_\phi(\hat{x}_i|z)] + D_{\text{KL}}(q_\theta(z|x_i) || p(z)) \quad (6)$$

In practice, a typical prior distribution for z_i is the unit Gaussian, $\mathcal{N}(0, 1)$, and all latent variables are assumed to be independent.

The benefit of using a VAE with a Gaussian prior is that each point on the data manifold is encoded into a Gaussian distribution in the latent space as opposed to an individual point. Then loosely speaking, the distribution on the latent space embedding follows a Gaussian mixture model. This promotes continuity in the latent space embedding, which is important for interpolating between data. Additionally, with each embedded point corresponding to something near a unit Gaussian, data generation can be reliably performed by decoding a sample from the unit Gaussian distribution.

A.2 Parallel Transport Networks

A.2.1 Parallel Transport Networks

The parallel transport convolution network (PTCNet) introduced the eponymous convolution in [36]. Previous local patch-based methods in [5, 33] defined filters locally without making it apparent how to consistently translate the kernel at vertex v_i to v_j . This means that the local frame of the kernel corresponds to global vector fields with many discontinuities. The discontinuities are precisely what PTCNet rectifies.

If we denote $(P_{p_0}^{p_i})(\cdot) : T\mathcal{M}_{p_0} \rightarrow T\mathcal{M}_{p_i}$ as the parallel transportation of a vector from the tangent plane at p_0 to the tangent plane at p_i then the discretized PTC of a compactly supported filter $k(x_0, \cdot)$ with a signal $f : \mathcal{M} \rightarrow \mathbb{R}$ is given by:

$$(f *_{\mathcal{M}} k) = \int_{\mathcal{M}} k(p_0, \exp_{p_0} \circ (P_{p_0}^{p_i})^{-1} \circ \exp_{p_i}^{-1}(p_i)) f(x) \text{dvol}(x) \quad (7)$$

$$\approx \sum_{j \in \mathcal{N}_i} k(p_0, \exp_{p_0} \circ (P_{p_0}^{p_i})^{-1} \circ \exp_{p_i}^{-1}(p_i)) m(p_i) f_i, \quad (8)$$

where \exp_{p_0} is the exponential map at p_0 and $m(p_i)$ is the local mass element. In discretization, the kernel at p_0 is mapped to a template points sampled in the tangent plane $T_{p_0}\mathcal{M}$, transported to the tangent plane at the relevant vertex v_i , and then mapped onto a local neighborhood about p_i on the surface \mathcal{M} . Practically, the kernel k is chosen to be a linear interpolate of a set of fixed stencil points. Then a PTC network layer can be written as the form,

$$\sigma(f *_{\mathcal{M}} k) = \sigma(\mathbf{W} \mathbf{F} \mathbf{M} f) \quad (9)$$

where $\mathbf{W} \in \mathbb{R}^{F' \times K}$ are the (learnable) convolutional weights, \mathbf{F} is the precomputed (fixed) interpolation weights, and \mathbf{M} is the mass matrix associated with the mesh. Additionally, σ denotes the nonlinear activation function for the convolutional layer.

The operator $P_{p_0}^{p_i}$ requires a pre-defined vector field to produce local frames on the manifold. In the original work, [36] determines this vector field as the gradient of the geodesic distance function on the mesh \mathcal{M} . Thus, this requires the choice of a *seed point* on the mesh with which to compute the distance to. Then the first axis of the local frame

corresponds to the gradient of the geodesic, while the second axis corresponds to the cross product of this gradient and the surface normal. Motivated by [5] which defines frames via principal directions of curvature, in our work, we use the first principal lines of curvature to define our vector field. To do this, we use the geodesic vector field to fix the ambiguity in the first principal directions of curvature so that both vectors lie in the same half-plane. We note that this global ambiguity is not necessarily resolved in [5].

B Framework for Disentanglement via Geometry

As discussed in the paper, the Fundamental Theorem of Surfaces motivates the use of our conformal factor and normal (CFAN) feature. To this point, we will formally state this theorem also known as the Bonnet Theorem. From this theorem, we will see that CFAN is essentially approximating the solution to a difficult system of partial differential equations known as the Gauss-Codazzi equations to reconstruct encoded surfaces. To establish this, we first introduce important geometric objects known as the fundamental forms. We refer to [14] as the standard reference in classical differential geometry.

B.1 Fundamental Forms

One of the most important concepts in the differential geometry of surfaces is that of fundamental forms. The first and second fundamental forms define the metric and embedded properties of a surface. We will define and relate these fundamental forms to identity and pose.

B.1.1 First Fundamental Form

The first fundamental form is critical for understanding metric properties of a surface. It is used to determine the arclength of a curve on a surface. Additionally, it is used to determine the local angle between curves on a surface.

Consider the point p on the surface \mathcal{M} . Assuming the surface is regular, there exists some local parameterization of the surface, $r(u, v)$. Then $\{r_u, r_v\}$ is a natural basis on the tangent plane to the surface at point p , $T_p(\mathcal{M})$. Now consider two tangent vectors, $u_1 = (a, b)$ and $u_2 = (c, d)$, where coordinates are with respect to the local basis. Then the inner product of these vectors is defined with the first fundamental form, I , as

$$I_p(u_1, u_2) = \begin{bmatrix} a & b \end{bmatrix} \begin{bmatrix} E & F \\ F & G \end{bmatrix} \begin{bmatrix} c \\ d \end{bmatrix} \quad \text{where} \quad E = r_u \cdot r_u, F = r_u \cdot r_v, G = r_v \cdot r_v. \quad (10)$$

As in Euclidean space, the inner product is precisely what gives a concept of length, area, and angle. This matrix is also denoted as g and referred to as the metric tensor. For a standard basis in Euclidean space, the metric tensor is simply the identity, I .

Now we consider what it means for two surfaces to share the same identity. A reasonable expectation is that local angle and local surface area will be the same for both surfaces if they have the same identity. Under this expectation, these surfaces are isometric and share the same first fundamental form. Thus, we appeal to the first fundamental form when evaluating the identity of a mesh.

It is important to stress that this expectation assumes that a surface cannot go under any elastic deformation without altering the identity as this changes the metric. So this framework is not appropriate for certain datasets such as meshes of human face expression, as a change in expression involves relatively large scale elastic deformations of the face.

B.1.2 Second Fundamental Form

We start by motivating the second fundamental form. Let $z = r_3(u, v)$ be a surface where the uv -plane is tangent to the surface at the origin. Then the Taylor expansion of z about the origin is

$$z = \frac{1}{2} \begin{bmatrix} u & v \end{bmatrix} \begin{bmatrix} L & M \\ M & N \end{bmatrix} \begin{bmatrix} u \\ v \end{bmatrix} + \text{h.o.t.} \quad (11)$$

$$\text{where} \quad L = r_{uu} \cdot \mathbf{n}, M = r_{uv} \cdot \mathbf{n}, N = r_{vv} \cdot \mathbf{n}$$

with \mathbf{n} denoting the surface normal at the origin. Then, the matrix in the equation, II_p , is referred to as the second fundamental form. Intuitively, the second fundamental form represents the second order deviation of the surface from the tangent plane at a given point.

Clearly, the second fundamental form depends on the surface normal \mathbf{n} . Due to its dependence on the embedding of the surface in the ambient space, \mathbb{R}^3 , the second fundamental form is not an intrinsic geometric property of the surface, and

is hence extrinsic. This is unlike the first fundamental form which is invariant under the ambient embedding of the surface. We associate this embedding into Euclidean space with the pose of the surface.

B.2 Gauss-Codazzi Equations

Before we can introduce the fundamental theorem, we must first define the Gauss-Codazzi equations. The Gauss equations consist of

$$\begin{aligned} EK &= (\Gamma_{11}^1)_2 - (\Gamma_{12}^2)_1 + \Gamma_{11}^1 \Gamma_{12}^2 + \Gamma_{11}^2 \Gamma_{22}^2 - \Gamma_{12}^1 \Gamma_{11}^2 - (\Gamma_{12}^2)^2 \\ FK &= (\Gamma_{12}^1)_1 - (\Gamma_{11}^1)_2 + \Gamma_{12}^2 \Gamma_{12}^1 - \Gamma_{11}^2 \Gamma_{22}^1 \\ FK &= (\Gamma_{12}^2)_2 - (\Gamma_{22}^2)_1 + \Gamma_{12}^1 \Gamma_{12}^2 - \Gamma_{22}^1 \Gamma_{11}^2 \\ GK &= (\Gamma_{22}^1)_1 - (\Gamma_{12}^1)_2 + \Gamma_{22}^2 \Gamma_{11}^1 + \Gamma_{22}^2 \Gamma_{12}^1 - \Gamma_{12}^2 \Gamma_{22}^1 - (\Gamma_{12}^1)^2. \end{aligned} \quad (12)$$

where $K := \frac{LN - M^2}{EG - F^2}$

In terms of classical differential geometry, the Codazzi-Mainardi equations are defined as

$$\begin{aligned} L_v - M_u &= L\Gamma_{12}^1 + M(\Gamma_{12}^2 - \Gamma_{11}^1) - N\Gamma_{11}^2 \\ M_v - N_u &= L\Gamma_{22}^1 + M(\Gamma_{22}^2 - \Gamma_{12}^1) - N\Gamma_{12}^2. \end{aligned} \quad (13)$$

Together, these form the Gauss-Codazzi equations. Here Γ denotes the Christoffel symbols of the second kind. These symbols are defined using Einstein summation notation as

$$\Gamma_{kl}^i := \frac{1}{2} g^{im} \left(\frac{\partial g_{mk}}{\partial x^l} + \frac{\partial g_{ml}}{\partial x^k} - \frac{\partial g_{kl}}{\partial x^m} \right), \quad (14)$$

where g is the metric tensor, and $g^{im} := (g^{-1})_{im}$. The operator $\frac{\partial}{\partial x^i}$ refers to the partial derivative with respect to the i^{th} coordinate of the local basis. Also, we note that the Christoffel symbols are symmetric in their lower indices.

Since the metric tensor g and the first fundamental form I are synonymous, the Gauss-Codazzi equations is a system of partial differential equations in terms of the first and second fundamental forms. Now, we formally state Bonnet's classical result.

Theorem 1 (Fundamental Theorem of Surfaces) *Let U be a simply connected domain in \mathbb{R}^2 and let E, F, G, L, M , and N be functions in $C^\infty(U)$. Additionally, we assume E and $F > 0$, and $EG - F^2 > 0$. Lastly, these functions satisfy the Gauss-Codazzi equations (12, 13). Then there exists an immersion $f : U \rightarrow \mathbb{R}^3$ with first and second fundamental forms*

$$\begin{aligned} I &= Edu^2 + 2Fdudv + Gdv^2 \\ II &= Ldu^2 + 2Mdudv + Ndv^2. \end{aligned} \quad (15)$$

The immersion f is unique up to rotation and translation.

In total, this theorem establishes that a surface can be reconstructed up to rigid motion given its first and second fundamental forms. Additionally, these fundamental forms satisfy a compatibility conditions known as the Gauss-Codazzi equations. As established in the main body of the paper, for genus zero surfaces, the conformal factor with respect to some reference surface defines the first fundamental form of a surface up to scaling. Additionally, it is clear from equation 11 that the second fundamental form can be recovered from the first fundamental form and the surface normals. Thus, it follows that a genus zero surface can be reconstructed given the CFAN feature, assuming compatibility conditions are satisfied.

Though the fundamental theorem concludes that a surface can be reconstructed given its fundamental forms, it is hard to reconstruct this surface in practice. This is because the reconstruction depends on solving the Gauss-Codazzi equations which are clearly complex. To this end, CFAN-VAE can be viewed as approximating the solution to the Gauss-Codazzi equations, essentially solving this system of partial differential equations. With this, we gain a better understanding of the problem that CFAN-VAE is solving and a better appreciation for its performance.

C Additional Details on Experimental Setup

We provide more details on the SMAL dataset used in this work. As mentioned, [41] makes use of the SMPL model from [27] to generate data. SMPL is a skinning model which allows for the generation of synthetic data given a shape

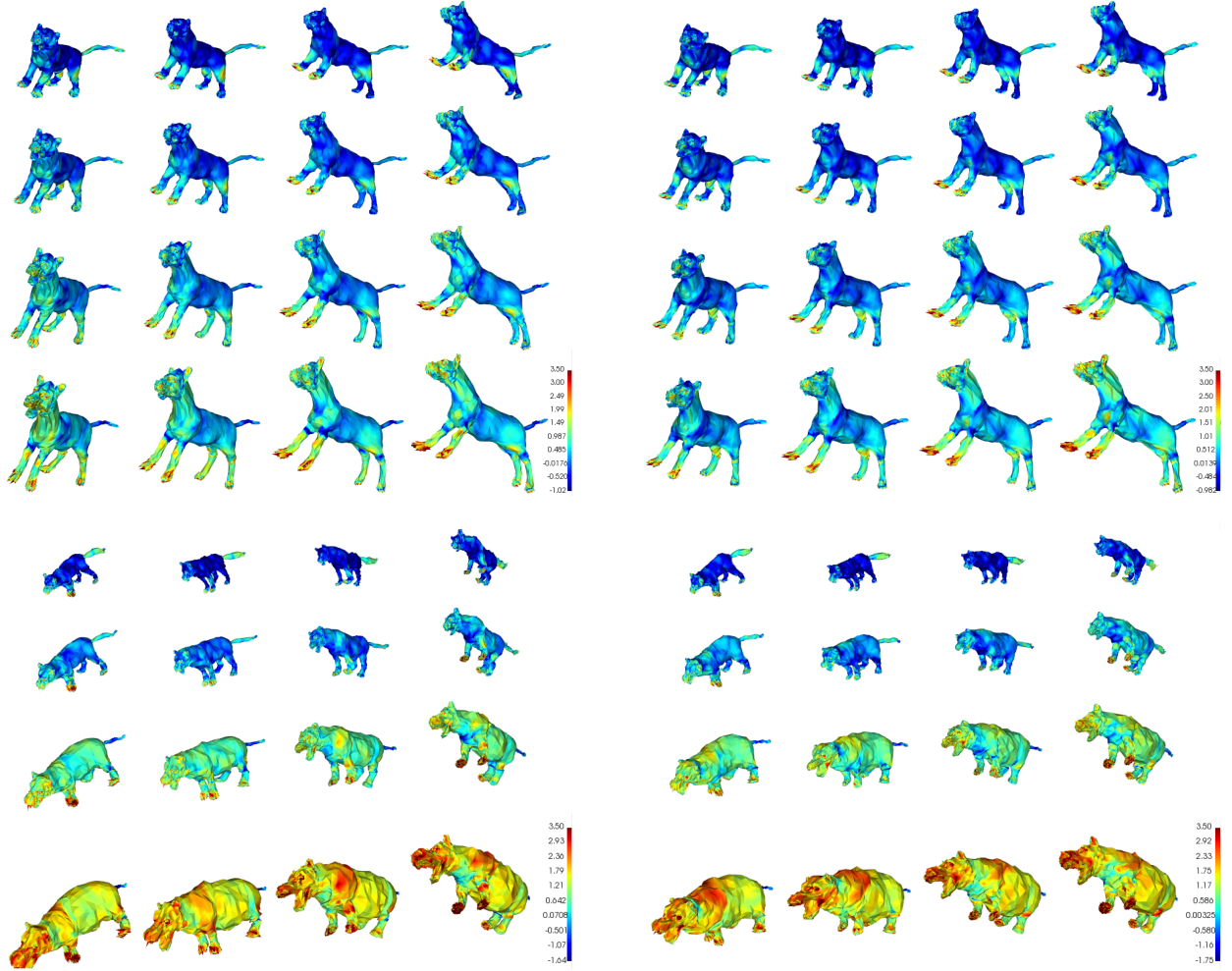


Figure 7: **Left/Right:** Additional interpolation instances on the SMAL dataset using the CFAN-VAE/registered xyz-VAE models as in Figure 1. The continued success of CFAN-VAE at geometric disentanglement is clear. Note the quality of the pose/identity transfer for CFAN-VAE is of higher quality in both cases. Unsupervised geometric disentanglement is present in the registered xyz-VAE, but not as strongly as in CFAN-VAE.

parameter and a pose parameter. In the SMAL dataset, we have a mean shape parameter associated with five classes of animals; cats, dogs, horses, cows, and hippos. We randomly sample 200 pose vectors from a normal distribution with standard deviation of 0.2. Additionally, we randomly sample 20 shape vectors from a normal distribution with standard deviation of 0.2. Then for each of the five classes we generate a mesh for each shape parameter, added to the mean shape parameter, and each pose parameter. These generated meshes are from what we form our training, validation, and test sets.

D Additional Figures

This section contains additional figures demonstrating the qualitative performance of CFAN-VAE. Specifically, we display additional instances of disentangled interpolation.

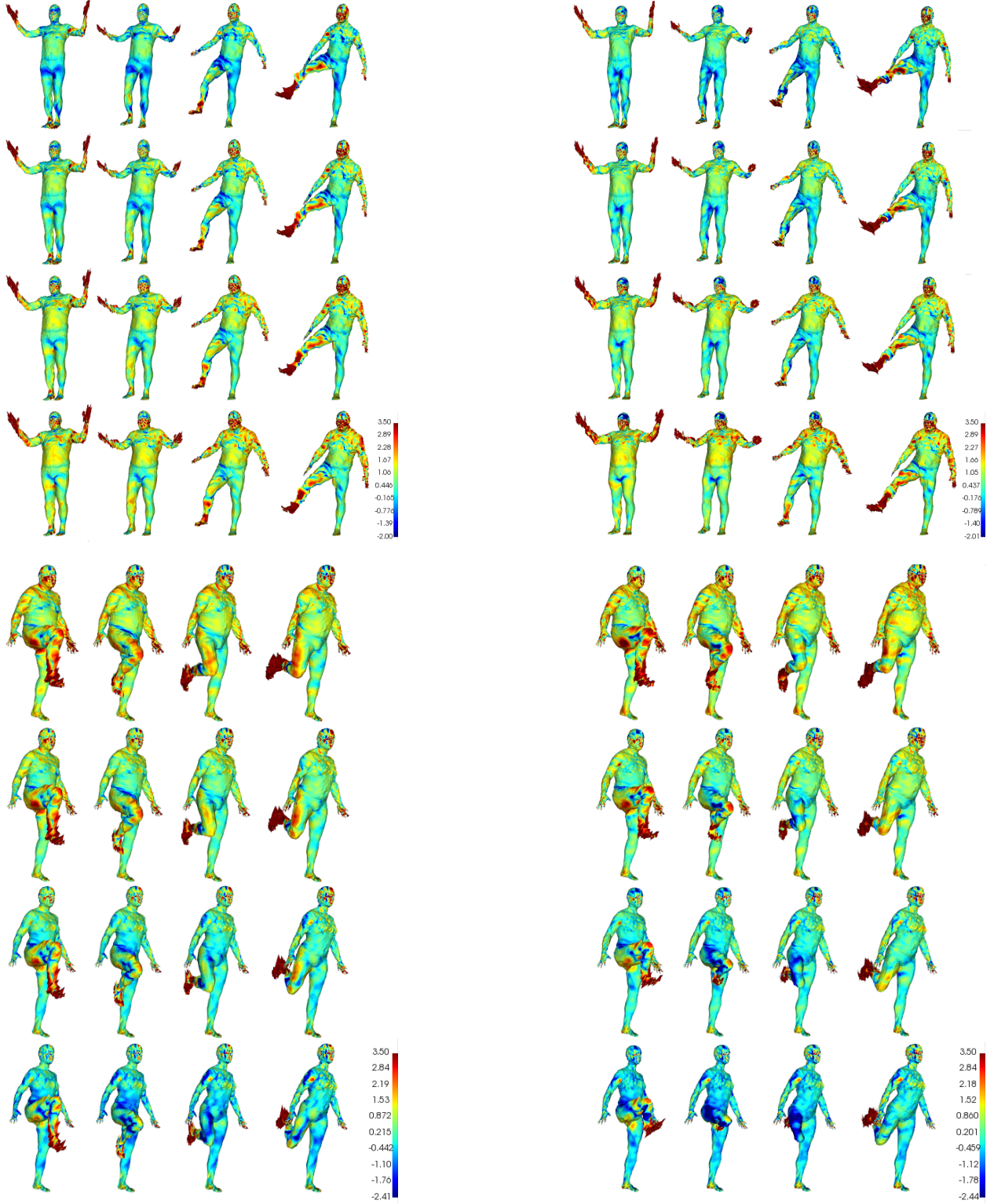


Figure 8: **Left/Right:** Additional interpolation instances on the DFAUST dataset using the CFAN-VAE/registered xyz-VAE models as in Figure 1. The continued success of CFAN-VAE at geometric disentanglement is clear. From the bottom right subfigure, it is apparent that some disentangled interpolations performed reliably by CFAN-VAE cannot always be performed with the registered xyz-VAE.